Estimation of Heat Sources Through Power Measurements in Thermal Models of PMSMs

Pablo Díaz-Brage, Antonio J. Rodríguez, Jon García-Urbieta, and Francisco González

***Abstract*—Electric powertrains are commonly used in the automotive industry nowadays. Thermal phenomena are critical for their performance, as the temperatures of some components must remain below certain thresholds during operation. This is the case of permanent-magnet synchronous motors (PMSMs): magnet temperatures cannot exceed a limit value to avoid demagnetization and motor failure. It is not possible, however, to directly monitor magnet temperatures by means of sensors. A feasible alternative to obtain this information consists of the use of virtual sensors, which fuse a numerical model of the motor with readings from a reduced set of physical sensors, for instance via the use of Kalman filters. The required models can be formulated using lumped-parameter thermal networks (LPTN), able to describe the thermal behavior of the motor in real time, at the cost of simplifying the representation of the thermal dynamics of the system. This simplification translates into parameter and geometry uncertainties, which can be alleviated by means of offline calibration. LPTNs are also sensitive to the heat sources in the system, and these, in turn, are highly dependent on the operation conditions. Although numerical models exist to describe heat source behavior, the accurate prediction of heat sources is challenging, particularly at the motor magnets. Improper modeling of thermal losses can result in unrealistic predictions of the motor temperatures. In this work, we present a method to estimate the internal temperatures of PMSMs using additional measurements of the motor power consumption. This information can be related to the thermal losses of the motor, helping Kalman filters to improve estimation accuracy. The proposed approach was tested with a benchmark example and in a standard Worldwide Harmonized Light Vehicles Test Procedure (WLTP) bench test with an automotive-grade PMSM. Results confirmed the ability of the method to correct the inaccuracies that stem from heat source uncertainties.**

***Index Terms*—eMotor, ePowertrain, heat source estimation, Kalman filter, lumped-parameter thermal network (LPTN).**

I. Introduction

MONITORING the thermal state of ePowertrains is a challenging task. It is critical to ensure that temperatures remain below certain thresholds to avoid damaging ePowetrain components [1]. In practice, however, due to economic and technical issues, it is often not feasible to place sensors at all sensitive locations to gather information about the system temperatures, and only data from a few thermocouples, often mounted near the external surfaces of the device, are available to infer the internal condition of the system. In the case of permanent-magnet synchronous motors (PMSMs), when magnet temperatures exceed limit values, demagnetization occurs, which results in irreversible damage to the drive [2]. To avoid this, a possibility is to use derating strategies based on the measured temperatures to limit the motor power. Such an approach benefits from the accurate knowledge of the relation between thermocouple readings and the actual temperatures of the motor hotspots [3], which is often achieved by means of the fusion of sensor data and a computational model of the thermal behavior of the drive [4], [5]. This model, in turn, frequently consists of a lumped-parameter thermal network (LPTN) that summarizes the thermal properties of the system and receives the heat generation in the drive as input, in the form of thermal losses. LPTNs are simplified thermal representations of the physical systems that they describe, and, as such, they are subjected to uncertainty. This can be alleviated, to a certain extent, by means of offline calibration procedures [6] that lead to an optimized set of LPTN parameters. The thermal losses that they receive as input, however, vary considerably during the operation and are typically described by analytical or empirical loss functions, as they cannot be directly measured with ordinary sensors. The use of such functions is complex in some cases, particularly for the iron and magnet losses [7], which are affected by rotating fields, temperature, or the switching frequency of the inverter [8], [9], [10], [11]. This represents a major source of uncertainty in the computational description of the PMSM and affects the reliability of the virtual sensing strategy.

Different approaches have been used to deal with this issue, including multiphysics modeling [12], neural networks [13], [14], [15], [16], [17] or magnet flux linkage observation [18], [19], [20], [21]. In a multiphysics approach, the PMSM model combines electromagnetic and thermal effects using high-fidelity techniques, obtaining accurate temperature calculations. However, this entails a high computational cost compared with LPTNs, which is a limitation for real-time applications. Regarding neural network approaches, they are applicable to the operational scenarios considered during their training. If they are used outside their training domain, neural networks can provide wrong estimations. Through the magnet

Received 28 September 2025; revised 26 December 2025; accepted 7 February 2026. Date of publication 11 February 2026; date of current version 27 May 2026. This work was supported by Galician Government under Grant ED431C 2023/01. *(Corresponding author: Antonio J. Rodríguez.)*

Pablo Díaz-Brage, Antonio J. Rodríguez, and Francisco González are with the Laboratorio de Ingeniería Mecánica, CITENI, Campus Industrial Ferrol, Universidade da Coruña, 15403 Ferrol, Spain (e-mail: pablo.diaz.brage@udc.es; antonio.rodriguez.gonzalez@udc.es; f.gonzalez@udc.es).

Jon García-Urbieta is with GKN Automotive Zumaia, 20750 Zumaia, Spain (e-mail: jon.garcia@gknautomotive.com).

Digital Object Identifier 10.1109/TTE.2026.3663688

flux observation, the magnet temperature can be derived by means of look-up tables or finite element models, although these require accurate model parameters [21].

These limitations can be overcome by fusing sensor data with an LPTN model of the PMSM. The efficiency of an LPTN allows real-time execution, and the use of sensor readings by means of a Kalman filter helps to overcome model uncertainties, yielding accurate estimations of the motor states. In addition, since the proposed approach is model-based, the solution can cover multiple scenarios, and it is not limited to a particular range of operation.

This article introduces a new method based on the extended Kalman filter (EKF) [22] that, thanks to the use of indirect power measurements, enhances the accuracy of virtual sensing. These measurements can be obtained from sensors that are often available in test benches, and could be retrieved as well from onboard sensing in practical applications, such as automotive powertrains. The proposed method can also be applied with different Kalman filter configurations. The method was demonstrated in the simulation of a benchmark *RC* thermal circuit, to highlight its operation and features. Afterward, it was applied to the temperature estimation of an automotive-grade PMSM mounted on a test bench. Results confirmed that it is possible to reduce the impact of heat loss uncertainty in experimental setups by means of indirect power measurements, improving the reliability of virtual sensors to determine the thermal state of electric drives.

II. Modeling and Estimation Methods

The LPTN models used in this research were built following the approach presented in [23]. The thermal state of the system is given by the dependent set of n variables

$$\mathbf{q} = \left[\mathbf{q}_\mathrm{T}^\mathrm{T} \;\; \mathbf{q}_\mathrm{Q}^\mathrm{T}\right]^\mathrm{T} \tag{1}$$

where $\mathbf{q}_\mathrm{T}$ contains the n_T temperatures of the LPTN nodes and $\mathbf{q}_\mathrm{Q}$, the n_Q heat flows through its components. These n variables are related by means of m algebraic constraints

$$\mathbf{\Phi}(\mathbf{q}, \mathbf{v}, t) = \mathbf{0} \tag{2}$$

that stem from Kirchhoff's equations and the constitutive equations of the components. In their general form, the constraints in (2) depend on time t and the system input $\mathbf{v}$, which includes heat sources and known temperatures. Besides, thermal capacitors introduce p linear ordinary differential equations in the form

$$\mathbf{\Gamma} = \mathbf{A}\dot{\mathbf{q}} + \mathbf{b} = \mathbf{0} \tag{3}$$

where $\mathbf{A}$ and $\mathbf{b}$ are a $p \times n$ matrix and a $p \times 1$ array, respectively. It can be shown [22] that it is possible to remove the constraints and express the dynamics in terms of a set of p independent variables $\mathbf{z}$ by means of the transformation

$$\mathbf{z} = \mathbf{B}\mathbf{q} \tag{4}$$

where $\mathbf{B}$ is a constant $p \times n$ matrix. An EKF is then used to perform a state and parameter estimation, where the augmented state vector takes the form

$$\mathbf{x} = \left[\mathbf{z}^\mathrm{T} \;\; \dot{\mathbf{z}}^\mathrm{T} \;\; \boldsymbol{\rho}^\mathrm{T}\right]^\mathrm{T}. \tag{5}$$

In (5), $\boldsymbol{\rho}$ is a set of o parameters to be estimated. These can include the physical properties of the LPTN components, such as resistance and thermal inertia, and also heat sources. The corresponding EKF prediction equations are

$$\mathbf{x}_{k+1} = \mathbf{F}_k\mathbf{x}_k + \mathbf{G}_k\mathbf{u}_k \tag{6}$$

$$\mathbf{h}_k = \mathbf{H}_k\mathbf{x}_k + \mathbf{N}_k\mathbf{u}_k \tag{7}$$

where $\mathbf{F}$, $\mathbf{G}$, $\mathbf{H}$, and $\mathbf{N}$ are state, input, output, and feedthrough matrices. Term $\mathbf{h}$ comprises the expression $\bar{\mathbf{h}}$ of s sensor readings in terms of the system variables, as well as the ODEs in (3), which enter the filter as perfect measurements

$$\mathbf{h} = \begin{bmatrix} \bar{\mathbf{h}} \\ \mathbf{\Gamma} \end{bmatrix} = \begin{bmatrix} \mathbf{C}\mathbf{q} \\ \mathbf{A}\dot{\mathbf{q}} + \mathbf{b} \end{bmatrix} \tag{8}$$

with $\mathbf{C}$ a constant $s \times n$ matrix. Term $\mathbf{u}$ stands for the filter input and verifies $\mathbf{u} = [\mathbf{v}^\mathrm{T} \;\; \dot{\mathbf{v}}^\mathrm{T}]^\mathrm{T}$.

The estimation strategy presented in [22] showed satisfactory results when estimating lumped parameters such as thermal resistance and inertia. The estimation of inputs, such as heat losses, however, was subjected to time delays related to the system inertia. The sensor data used for the estimation included only temperature readings, and changes in heat losses were not immediately translated into temperature variations because of the existence of thermal capacitors. In addition, there exist situations in which the filter does not have enough information to correctly estimate the temperatures in nodes where sensors have not been placed. When fusing sensor data and LPTN simulation results, the filter might deliver unrealistic values of heat flows in the circuit if the computational representation of heat losses is not accurate, as will be shown in Section III. This results in an estimator with high uncertainty regarding the temperature estimations in nodes without sensor readings, which is often the case of relevant spots in the drive, such as the magnets and the end-windings.

A workaround to this issue is using the overall energy balance of the motor to enforce a physics-based correction of heat flows by the filter. For example, the difference between the input that an eMotor receives as electric power and the mechanical power that returns as output is closely related to the heat losses in the drive. This work proposes to use this information to constrain the heat estimation carried out by the filter in such a way that the temperature estimation agrees with the energy balance of the system. To do so, term $\mathbf{h}$ in (8) is enlarged with a measurement of the energy balance of the system $\mathbf{h}_Q$

$$\mathbf{h} = \begin{bmatrix} \bar{\mathbf{h}} \\ \mathbf{h}_Q \\ \mathbf{\Gamma} \end{bmatrix} = \begin{bmatrix} \bar{\mathbf{h}} \\ P_\mathrm{i} - P_\mathrm{o} \\ \mathbf{\Gamma} \end{bmatrix} \tag{9}$$

where P_i and P_o are measurements of the power that the drive receives as input and returns as output, respectively. For a system with n_s heat sources given by Q_i, with $i = 1, \ldots, n_\mathrm{s}$, the power balance can be expressed as $P_\mathrm{i} - P_\mathrm{o} = \sum Q_i$ and used to determine the total heat losses of the system.

III. Benchmark Problem

The methods described in Section II were initially tested using a simple thermal *RC* circuit, shown in Fig. 1. This use

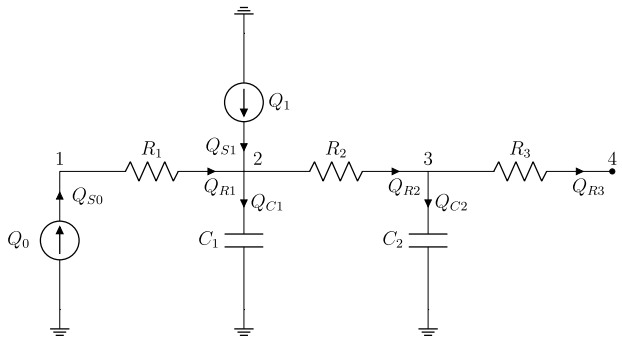

Fig. 1. Benchmark *RC* thermal circuit.

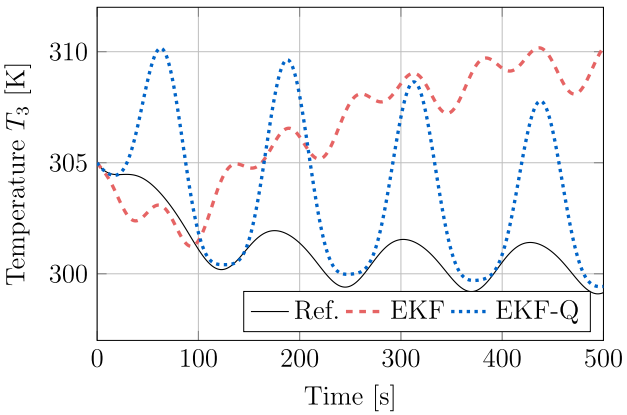

Fig. 2. *RC* benchmark: T_3 estimation with a sensor in node 1.

case is a benchmark problem, and all its parameters and the exact solution are known. Testing the method in a simple use case allows one to get a comprehensive analysis of its performance in different scenarios: parameter uncertainties, sensor location, sensor noise, etc. To represent the issues presented in Section I, the circuit consists of two heat sources, Q_0 and Q_1, connected to three resistors and two thermal capacitors. The system contains four nodes, of which number 4 represents air at a constant temperature $T_{\text{air}} = 300$ K.

The heat generated at each source follows a sinusoidal signal, $Q_0 = 10\sin(2\pi \cdot 8t/500 + \pi/2)$ W and $Q_1 = 30\sin(2\pi \cdot 4t/500) + \pi/2)$ W. The values of resistors R_1, R_2, and R_3 are 1, 2, and 3 K/W, respectively. The capacitors are $C_1 = 0.1$ J/K and $C_2 = 0.2$ J/K, and the initial temperatures of the nodes to which they are connected are set to $T_2^0 = 299$ K and $T_3^0 = 301$ K.

The test case is a 500-s simulation of the thermal dynamics of the *RC* circuit. A reference solution (Ref.) is generated using the known values of all lumped parameters and heat losses. Next, a defective model of the *RC* circuit is defined to test the estimation methods presented in Section II. Heat sources Q_0 and Q_1 in this model are assumed to be unknown, and only their initial values $Q_0 = 10$ W and $Q_1 = 30$ W are provided. An EKF defined by (5)–(8) is applied to this model to carry out the estimation of the heat sources and the state. Another extended filter (denoted as EKF-Q) is also formulated, replacing (8) with (9). Both filters have the following augmented state:

$$\mathbf{x} = \begin{bmatrix} T_2 & T_3 & \dot{T}_2 & \dot{T}_3 & Q_0 & Q_1 \end{bmatrix}^{\mathrm{T}} \tag{10}$$

where $\mathbf{z} = [T_2 \;\; T_3]^{\mathrm{T}}$ and $\boldsymbol{\rho} = [Q_0 \;\; Q_1]^{\mathrm{T}}$ are the heat sources to be estimated. These are modeled through a random walk, keeping their value equal to the one estimated in the previous time step

$$Q_{i,k+1} = Q_{i,k} + \zeta \tag{11}$$

where ζ is white noise. The corresponding state matrix is

$$\mathbf{F} = \begin{bmatrix} \mathbf{F_z} & \mathbf{0}_{2p\times 2p} \\ \mathbf{0}_{o\times 2p} & \mathbf{I}_{o\times o} \end{bmatrix} \tag{12}$$

where $\mathbf{F_z}$ is the state matrix that corresponds to the independent variables and their derivatives, whose expression can be found in [22], and $\mathbf{I}$ is the identity matrix.

Three sensors are considered to retrieve measurements from the *RC* circuit: temperature sensors in nodes 1 and 2, and the instantaneous power balance of the system. For the temperature sensors, three combinations are defined: sensor in node 1 active, sensor in node 2 active, and both active. If all sensors are active, the full term of sensor readings is

$$\mathbf{o} = \begin{bmatrix} \mathrm{T}_1^{\mathrm{s}} & \mathrm{T}_2^{\mathrm{s}} & P_{\mathrm{i}} - P_{\mathrm{o}} \end{bmatrix}^{\mathrm{T}}. \tag{13}$$

All sensors are considered to be ideal. The purpose of the benchmark is to illustrate the operation of the EKF-Q filter, and so it is assumed that temperatures and the total power balance are accurately measured. Results and discussion for each test case are shown next.

A. Sensor in Node 1

If a single temperature sensor at node 1 is used, heat sources Q_0 and Q_1 cannot be determined. This results, for instance, in both filters rendering inaccurate estimations of the temperature T_3, as shown in Fig. 2. However, it must be noted that the value of T_3 delivered by the EKF-Q filter follows the same trend as the reference, although with different values. Conversely, the temperature estimated by the conventional EKF diverges because there is no constraint on the total amount of heat that can be introduced in the system in the estimation of the heat sources. The EKF-Q ensures that the sum of the heat losses, $Q_0 + Q_1$, equals the real heat flow into the system, although the limited sensor information about temperatures makes it impossible to determine the exact amount of heat that corresponds to each source. This, in turn, affects the estimation of temperatures in nodes 2 and 3.

B. Sensor in Node 2

This case also considers a single temperature sensor, located now at node 2. The uncertainty about the heat sources decreases because the temperature of node 2 is related to the overall heat input in the system. The estimation delivered by the EKF, however, is not completely accurate and it includes a certain delay with respect to the reference solution, as can be seen in Fig. 3. When using the EKF-Q, temperature T_3 can be accurately estimated, since the knowledge of T_2 and the total heat flowthrough the circuit makes the temperature of node 3 completely determined. However, as in the previous case,

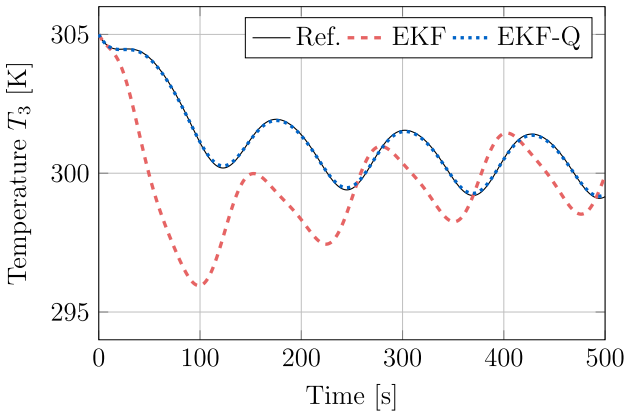

Fig. 3. *RC* benchmark: T_3 estimation with a sensor in node 2.

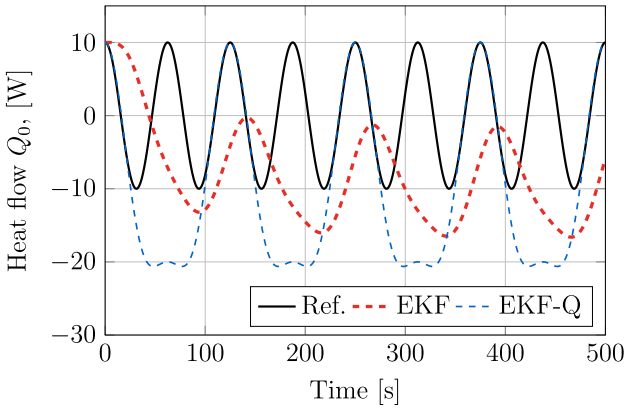

Fig. 4. *RC* benchmark: Q_0 estimation with a sensor in node 2.

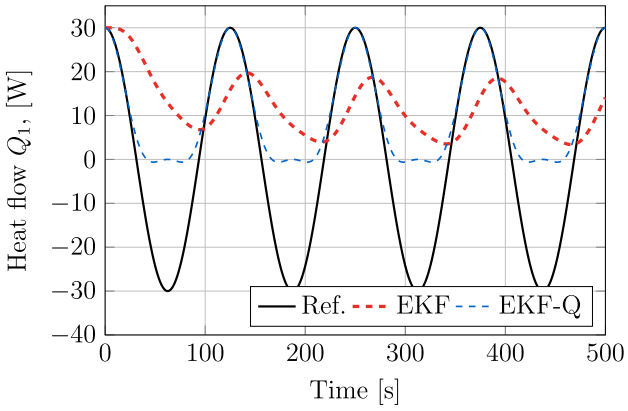

Fig. 5. *RC* benchmark: Q_1 estimation with a sensor in node 2.

none of the filters can estimate the value of each heat source, as shown in Figs. 4 and 5, which affects the estimation of the temperature in node 1. If only one source was uncertain, the EKF-Q could also be used to determine T_1.

C. Sensors in Nodes 1 and 2

To provide more information to the filter, two temperature sensors are placed in nodes 1 and 2. The estimation of T_3 is shown in Fig. 6. Even in this situation, the EKF cannot properly estimate the temperature in node 3. The knowledge of the temperatures in nodes 1 and 2 allows this filter to determine the correct value of the heat source Q_0. The value of Q_1, however, remains undetermined, because it cannot be directly evaluated from the temperature of nodes 1 and 2. However, when the total heat flow that enters the system is known, it is possible to obtain the right value of Q_1. Accordingly, the EKF-Q is able to accurately estimate all the unknowns of the benchmark circuit, namely, both heat sources and the temperature of node 3.

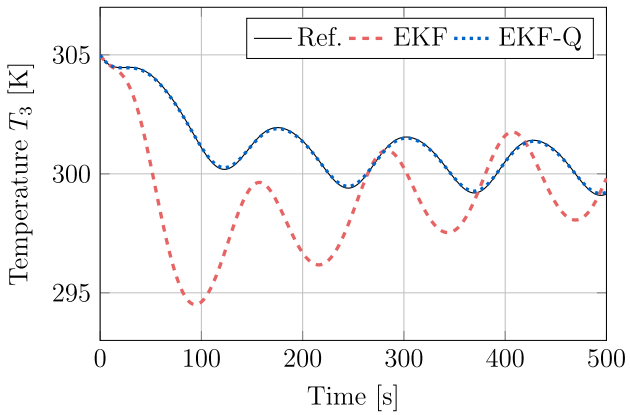

Fig. 6. *RC* benchmark: T_3 estimation with sensors in nodes 1 and 2.

D. Measurement Noise Analysis

An important factor in the accuracy of the estimations is related to the quality of the sensors installed. In the previous experiments, the sensors employed were ideal. In real scenarios, however, the sensor measurements are affected by noise that can degrade the accuracy of the estimation.

To evaluate the robustness of the proposed method to sensor noise, the benchmark simulation is repeated with different noise levels for the temperature sensors and the instantaneous power balance. White noise, i.e., noise with a zero mean and a finite standard deviation (σ), was added to the measurements, with three different standard deviations considered for the temperature and power measurements, respectively: 0.5 K and 0.5 W, 1.0 K and 1.0 W, and 5.0 K and 5.0 W.

The noise analysis is focused on the scenario with a sensor in node 2, since it provides accurate temperature estimations while having a minimal amount of sensors. Fig. 7 presents the temperature measurements in node 2 under different noise levels, together with the reference value and the temperature estimation for node 2. As the noise increases, the estimated value deviates further from the reference value while still tracking its trend.

The deviation in the estimated T_2 shown in Fig. 7 has an effect on the estimation of the temperature in node 3, which does not have any sensor installed. The results in Fig. 8 show that the estimation error increases with sensor noise. However, the increment of the error remains below the noise levels added to the sensors, which means that the EKF-Q can still improve estimation quality when using noisy sensors.

E. Initial Temperature Error

Another parameter which is difficult to determine is the initial temperature of the different parts of the system. To test the

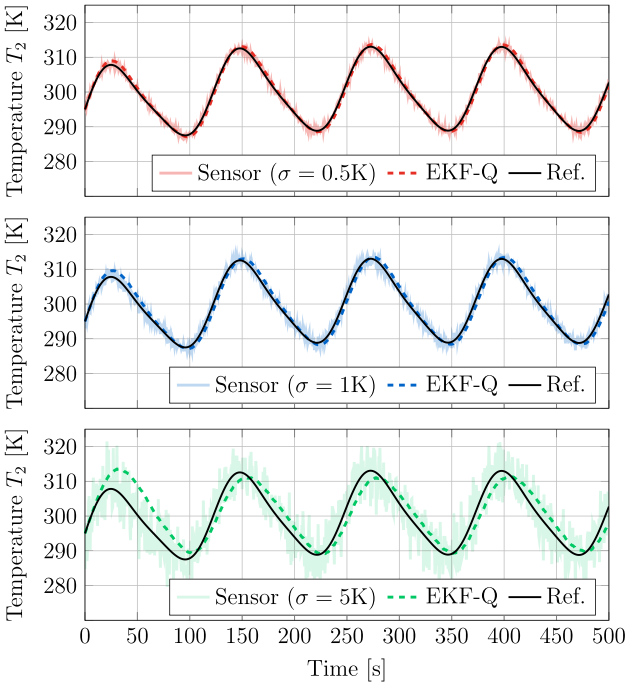

Fig. 7. *RC* benchmark: T_2 estimation with sensor in node 2 under different noise levels.

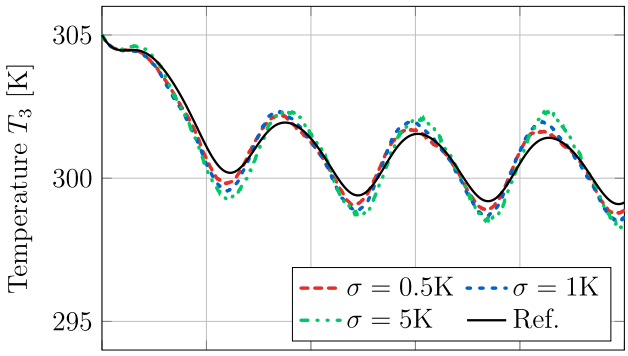

Fig. 8. *RC* benchmark: T_3 estimation with sensor in node 2 under different noise levels.

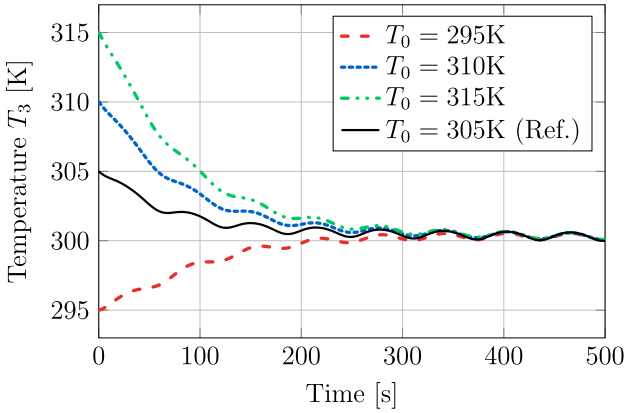

Fig. 9. *RC* benchmark: T_3 estimation with sensor in node 2 under different initial temperatures.

performance of the proposed method to these uncertainties, the benchmark was run starting from three different temperatures at the nodes connected to capacitors (nodes 2 and 3). Results

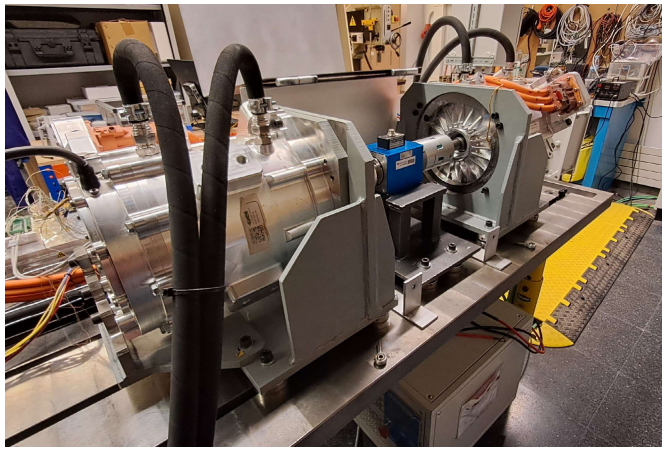

Fig. 10. Back-to-back configuration used in the test bench.

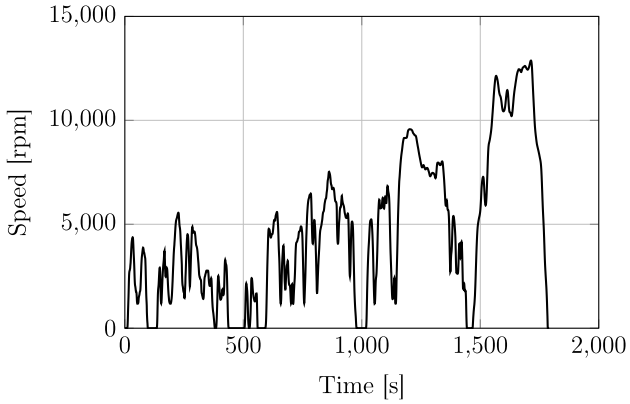

Fig. 11. Speed of the eMotor during the WLTP cycle.

are compared to the reference simulation in Fig. 9. It can be seen how the method is able to correct the initial error after some time.

IV. Example: Automotive-Grade PMSM

The proposed method was also applied to the estimation of internal temperatures in a PMSM eMotor used in automotive powertrains. In this context, it is of importance to track the temperature of the motor in its different parts: excessive overheating can cause a critical failure in the device. Even if permanent damage does not occur, the performance of the electric motor is affected by its operating temperature. Since it is not feasible to install thermal sensors in the critical locations of the motor in production vehicles due to cost, complexity, and the need for wireless data transmission from rotating parts [3], [4], [5], [11], estimation becomes the basis to retrieve this information.

The eMotor employed in this work is shown in Fig. 10. The device under test (DUT) was mounted on a test bench, where it was connected in a back-to-back configuration to another eMotor (load), mechanically coupled by a torque sensor between their shafts. The DUT has a maximum continuous power of 92 kW and a peak power of 140 kW. It was operated in torque control mode to emulate real driving conditions, while the load motor was operated in speed control mode to

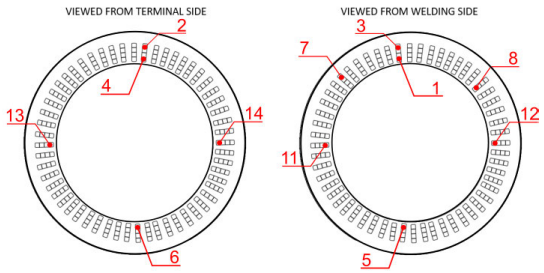

Fig. 12. Location of the sensors in the stator: B-side end-winding (left) and A-side end-winding (right).

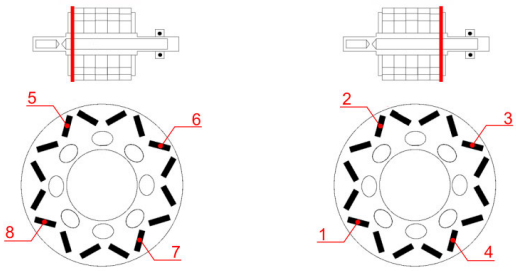

Fig. 13. Location of the sensors in the rotor.

impose dynamic profiles such as the Worldwide Harmonized Light Vehicles Test Procedure (WLTP) cycle (Fig. 11). Each motor was driven by its own inverter connected to a DC supply, enabling independent control and energy recirculation between motors. Mechanical power was calculated using the torque sensor and motor resolvers, while electrical power was measured via current and voltage sensors. The angular velocity of the selected motor during this cycle is shown in Fig. 11.

Temperature measurements were obtained using Type K thermocouples IEC 60584-1, with an accuracy of ± 1.5 °C, placed in three different locations: the A and B end-windings (used by the filter to perform the estimation) and the rotor magnets (for validation only), as shown in Figs. 12 and 13. The rotor-mounted sensor required wireless telemetry, which is feasible in laboratory conditions but not practical for production vehicles. Control and data acquisition were implemented via CAN bus, allowing real-time monitoring of torque, speed, electrical power, and temperature. It should be noted that both the rotor and stator sensors are mounted on the stacks highlighted in red in Fig. 13. Due to symmetry, it is expected that the sensors installed in each part will measure similar temperatures. In addition, the LPTN model cannot represent the temperature distribution over the surface. Therefore, for the estimation, the sensors of each part are grouped into one unique measurement, which corresponds to the maximum temperature measured in each part. This also means that, in a practical application such as a vehicle, only one temperature measurement per end-winding would be necessary. However, if the temperature is not uniformly distributed, the accuracy of the estimations could be affected.

The test bench also includes a torque transducer to measure the torque transmitted between both motors at the shaft. The angular speed is measured by the resolver of the eMotor. These two magnitudes are later used to compute the mechanical power delivered at the shaft. The electric magnitudes of the DUT are measured by means of current sensors, and the electrical power consumed by the DUT is obtained through a wattmeter. In a vehicle setup, an approximation of the torque could be obtained by means of the currents and the motor characteristics. Although it may not be as accurate as using a torque transducer, useful information regarding the mechanical power can be acquired.

The filters were built upon an LPTN model of the motor, which represents its main internal components: shaft, bearings, rotor, magnets, end-plates, end-rings, stator iron, active winding, end-windings, housing with heat extraction sinks, cooling jacket, and internal air cavities. A schematic of the LPTN is shown in Fig. 14, illustrating the heat transfer paths between these parts. Solid lines indicate conduction, while dashed lines represent convection.

The LPTN consists of 23 nodes and a total of 60 components, including thermal resistors, capacitors, and heat sources. There are 22 constant-value resistors, representing the heat transfer by conduction, 15 variable resistors representing convection, and 10 thermal capacitors. The value of their resistance and inertia was optimized following the approach described in [2] and [6]. Through sensitivity analysis, the most relevant parameters were identified and later optimized based on a certain set of experimental service tests of the motor. The heat losses were described by 13 sources that account for the electromagnetic and mechanical effects inside the drive. They were modeled using commercial multiphysics simulation software. Two locations concentrated the most relevant uncertainties in heat generation, namely the rotor magnets and the end-winding rack. Heat generation at the magnets is assumed to follow a semi-empirical law. The thermal losses at the rack, conversely, are completely unknown and are represented in the LPTN with a zero-valued heat source.

Even though the optimization process led to an improved LPTN representation of the motor, its operation was still subjected to uncertainties. The value of thermal resistors experiences variations over time, and the heat sources description does not completely capture dynamic effects during operation. The main role of the estimation filters is to overcome these model limitations using data provided by the sensors mounted on the system. In this work, only two thermocouples were used to this end, namely the ones installed at the end-windings. The sensor in the rotor magnet was used to validate the estimation results. Rotor-located sensors require wireless data retrieval, which would make it difficult to use them in practical automotive applications, so they were employed for verification only and are not part of the estimation solution.

To enable the EKF-Q solution, the total heat losses during operation were obtained from the power balance of the DUT. The mechanical power P_{m} transmitted at the shaft was determined using the readings of the torque sensor between the motors and their angular velocity, provided by the motor resolvers. The electric power P_{e} provided to the DUT was obtained from the voltage readings of its inverter and current probes. The total heat input into the LPTN can be approximated by the difference between these two power values.

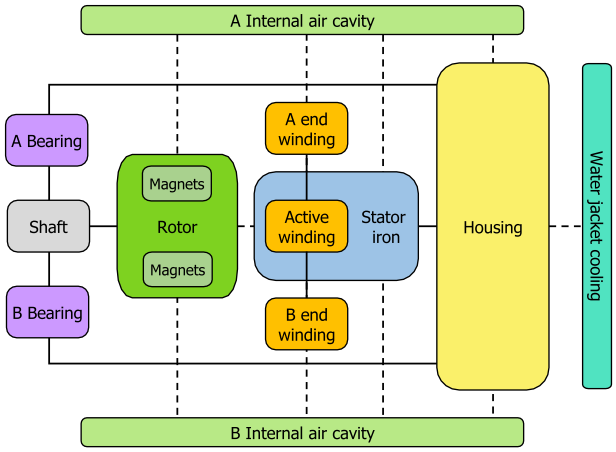

Fig. 14. Conceptual division of the eMotor for LPTN model construction.

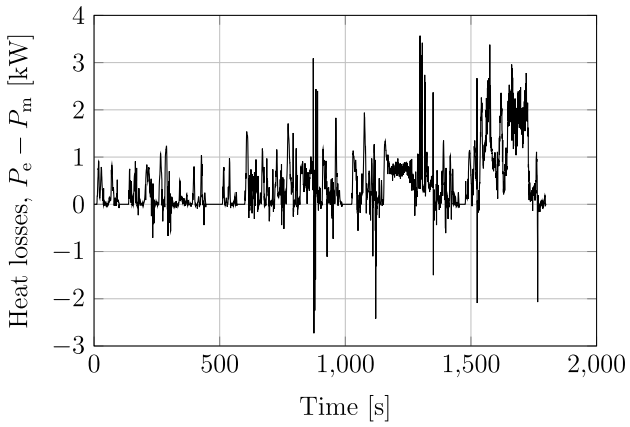

Fig. 15. PMSM: difference between input electric power P_e and output mechanical power P_m measured during a WLTP cycle.

In practice, the power balance in the DUT adds a single sensor to the filter. As shown in Section III, the number and location of the sensors affect the identification of the individual heat sources. As a consequence, not all 13 heat sources in the LPTN can be estimated. Instead, the two most uncertain values, i.e., the magnet and rack losses, were marked for estimation, while the other sources are driven by their model. The augmented state vector of the Kalman filters in this use case is

$$\mathbf{x} = \left[\mathbf{z}^{\mathrm{T}} \;\; \dot{\mathbf{z}}^{\mathrm{T}} \;\; \mathbf{Q}^{\mathrm{T}}\right]^{\mathrm{T}} \tag{14}$$

where $\mathbf{z}$ includes the temperature of the nodes connected to thermal capacitors and $\mathbf{Q}$ is a 2×1 term that contains the heat losses in the magnet, Q_m, and the rack, Q_r. The sensor readings of the EKF-Q are

$$\mathbf{o} = [T_A \;\; T_B \;\; P_e - P_m]^{\mathrm{T}} \tag{15}$$

where T_A and T_B stand for the temperature in the end-windings A and B, respectively. These temperatures are the only sensor data available to the EKF. The power difference in (15) can be related to the thermal losses in the magnet and rack by means of

$$\hat{Q}_m + \hat{Q}_r = P_e - P_m - \sum Q_j \tag{16}$$

where term Q_j includes the remaining 11 heat sources that are not being estimated by the filter. Symbol $\hat{}$ indicates that the terms on the left-hand side are approximations that result from the combination of real sensor measurements and variables obtained through mathematical models.

A. Results

To evaluate the performance of the proposed filters, estimated temperatures were compared to thermocouple measurements at the end-windings A and B, and at the magnets. Two different use cases were tested: estimation of the rack source alone and joint estimation of the rack and magnet sources. Both test cases can be performed on the results of each experimental run of the WLTP cycle. If both sources are estimated, the original expressions of (14) and (16) are used. If just the heat at the rack is estimated, term $\mathbf{Q}$ only includes source Q_r and term $\hat{Q}_m$ is added to $\sum Q_j$ in (16). Fig. 15 shows the difference between input and output power at the DUT during a WLTP cycle. This information is used by the EKF-Q filter in both test cases. It must be mentioned that, during some parts of the WLTP cycle, the DUT is dragged by the load device and acts as a generator, resulting in negative values of $P_e - P_m$. These negative values do not represent an actual removal of heat from the LPTN, because thermal losses still exist when the device works as a generator. Hence, the absolute value of the difference is used in (16).

The results from the *RC* benchmark can shed some light on the effect of sensor location and noise. The benchmark shows that the sensor location has a direct impact on the estimation accuracy: the closer the sensors are to the nodes of interest, the higher the accuracy will be achieved. For instance, if the sensors are located in the housing, the estimation will be more dependent on how the elements between the housing and the magnet are modeled. With respect to sensor quality, more noise in the measurement turns into a reduction in the accuracy of the estimation, although the fusion with the LPTN model helps to minimize this effect.

In all the estimations of this example, the covariance matrices of the plant noise $\mathbf{\Sigma}$ and measurement noise $\mathbf{R}$ have been adjusted manually. The measurement noise matrix can be easily adjusted using values close to the noise values specified in the sensor data sheet. The plant noise matrix is more complex to adjust, since it covers the modeling errors, which are usually unknown. Its calculation involves a trial-and-error procedure, which usually consists of starting with low values, giving more confidence to the model, and increasing these values until the sensor corrections lead to a convergence in the estimations. It should be noted that there are some methods for the online estimation of covariance matrices [22], [24], [25], [26], but they are not discussed in this work for simplicity.

After the adjustment procedure, matrix $\mathbf{\Sigma}$ is a diagonal matrix with a value of $2 \cdot 10^{-5}\mathrm{K}^2$ for the states of the system (temperatures and their derivatives) and of $1 \cdot 10^{-3}\mathrm{W}^2$ for the rack and magnet heat sources, respectively. Matrix $\mathbf{R}$ is also a diagonal matrix whose elements are set to $0.5\mathrm{K}^2$ for the thermocouples and $1\ \mathrm{W}^2$ for the measurement of the total heat losses, $P_e - P_m$.

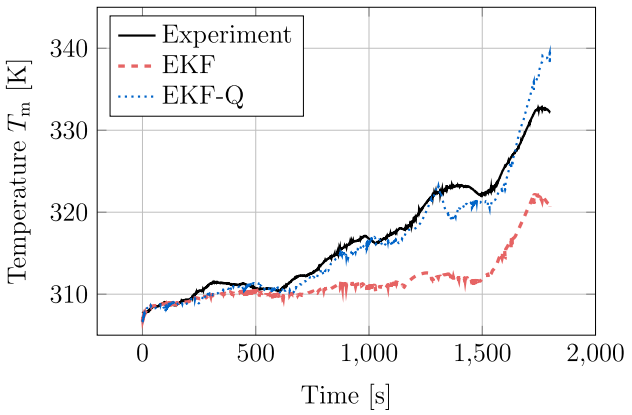

Fig. 16. PMSM: Magnet temperature during a WLTP cycle with $\mathbf{Q} = [Q_r]$.

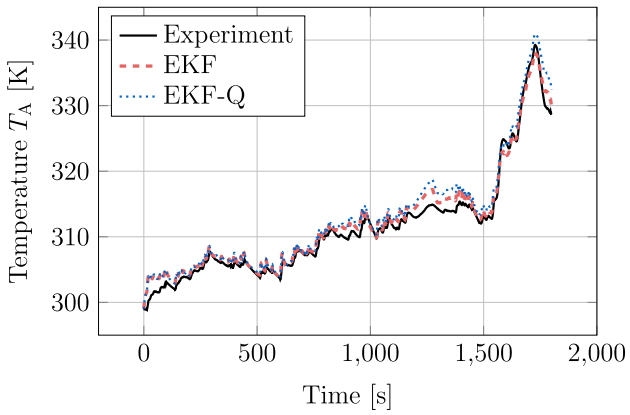

Fig. 17. PMSM: End-winding A temperature during a WLTP cycle with $\mathbf{Q} = [Q_r]$.

TABLE I
PMSM: ERRORS IN THE ESTIMATIONS DURING A WLTP CYCLE WITH $\mathbf{Q} = [Q_r]$

	Heat losses [kW]		T_m [K]		T_A [K]	
	RMSE	Peak	RMSE	Peak	RMSE	Peak
EKF	0.4375	2.8742	6.5341	11.689	1.1878	3.9132
EKF-Q	0.3415	2.6287	1.6649	7.3529	1.7994	5.4007

The LPTN and the Kalman filter are integrated with a time step $h = 0.5$ s. All the experiments were simulated offline using sensor readings obtained from bench experiments. The method was implemented in C++ for computational efficiency, and the simulations were executed in one core in an Intel[1] Core[2] i7-8700 CPU @ 3.20 GHz with 16 GB of RAM. The total simulated time was 1800 s, which required an average elapsed time of 4.46 s in computations, which confirmed the real-time performance of the method.

1) Rack Heat Source Estimation: This case treats Q_r as the only unknown input to be estimated. Fig. 16 shows that the conventional EKF is unable to properly track temperature variations at the magnet. The EKF-Q improves this temperature estimation by relying on the information from the power balance depicted in Fig. 15. Table I shows the estimation errors in terms of the root-mean-square error (RMSE) and maximum error (peak).

Fig. 17 shows the temperature at end-winding A and provides an explanation for the comparatively poor behavior of the EKF in the estimation of magnet temperature. Temperature T_A can be directly compared to sensor readings, unlike T_m at the magnet. The Kalman filter uses this information to adjust the LPTN output and match the experimental results. Because temperature measurements at the magnets are not available, the temperature delivered by the filter at that location relies on proper definition and tuning of the LPTN and the correctness of the heat source models. Uncertainty in these heat sources translates into inaccurate results, as confirmed by Fig. 16, even after the adjustment of the LPTN.

[1]Registered trademark.
[2]Trademarked.

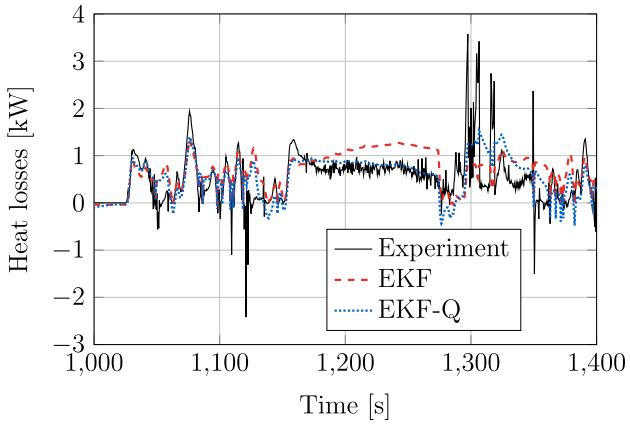

Fig. 18. Comparison of the total heat losses during the WLTP. The losses from experimental data ($P_e - P_m$) are compared with the total heat losses of the model obtained by each estimator ($\hat{Q}_r + \sum Q_j$).

The time-histories of total heat losses estimated by the filters are shown in Fig. 18. These are compared to the experimental measurement of $P_e - P_m$. For the sake of clarity, a 400-s interval of the experiment is illustrated. The value of Q_r estimated by the EKF is not backed by sensor data, and this leads to magnet temperature predictions below thermocouple readings.

The different behavior of EKF and EKF-Q can also be explained by considering the temperature of the end-windings evaluated in an open-loop simulation, shown in Fig. 19. Simulating the thermal dynamics of the motor using only its LPTN model predicts higher temperatures in the end-windings than those actually recorded by sensors. The EKF only receives temperature measurements from the end-windings, and its data fusion results in an overall decrease in the temperatures predicted by the LPTN alone. A side effect of this correction is the introduction of heat flows in the description of the thermal behavior that do not respond to the physical constraints of the system, resulting in lower magnet temperature. On the other hand, the EKF-Q has information regarding the total heat losses and, therefore, it can arrive at a solution in which node temperature correction does not come at the expense of

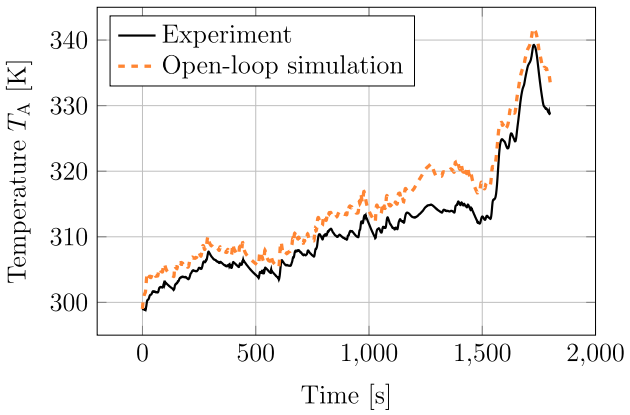

Fig. 19. PMSM: End-winding A temperature during WLTP cycle compared to an unfiltered open-loop simulation of its thermal dynamics.

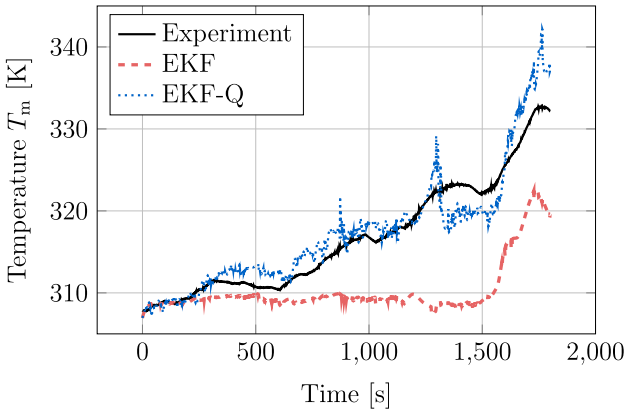

Fig. 20. PMSM: Magnet temperature during a WLTP cycle with $\mathbf{Q} = [Q_m \ Q_r]^T$.

TABLE II

PMSM: ERRORS IN THE ESTIMATIONS DURING A WLTP CYCLE WITH $\mathbf{Q} = [Q_m \ Q_r]^T$

	Heat losses [kW]		T_m [K]		T_A [K]	
	RMSE	Peak	RMSE	Peak	RMSE	Peak
EKF	0.4248	2.7890	8.1169	15.028	0.6725	3.6202
EKF-Q	0.3329	2.6780	2.3631	9.6704	1.4814	5.1594

introducing heat losses in the system dynamics that are not based on the physical phenomena inside the drive.

2) Magnet and Rack Heat Source Estimation: In this case, $\mathbf{Q} = [Q_m \quad Q_r]^T$; the corresponding magnet temperature estimation is shown in Fig. 20. The estimation errors in this scenario are summarized in Table II.

Again, the EKF is unable to properly track temperature variations in the motor magnets. The estimation of two heat sources further deteriorates temperature predictions. The EKF-Q, conversely, is able to track dynamic variations in magnet temperature, although the estimation is not as accurate as in the previous test case, as can be seen by comparing the residuals from Tables I and II. Also, the corrections performed by the EKF-Q come at the expense of introducing differences with respect to sensor readings at the end-windings, as can be seen in Fig. 21. The heat losses predicted by each estimator were very similar to those depicted in Fig. 18.

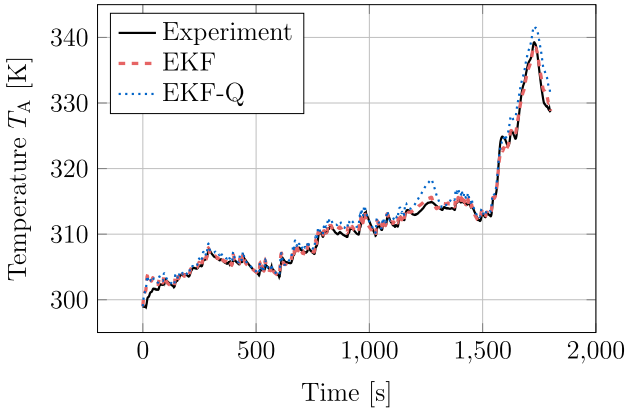

Fig. 21. PMSM: End-winding A temperature during a WLTP cycle with $\mathbf{Q} = [Q_m \ Q_r]^T$.

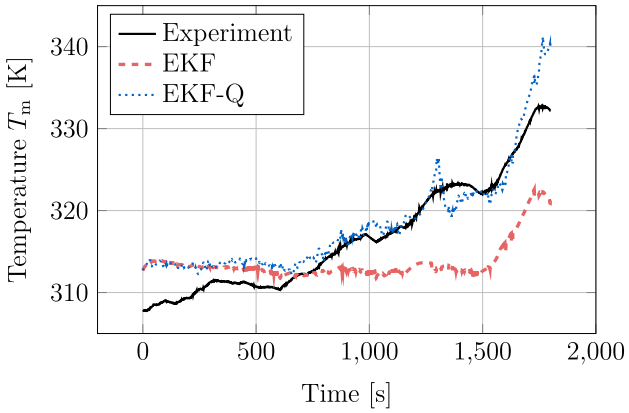

Fig. 22. PMSM: Magnet temperature during a WLTP cycle with $\mathbf{Q} = [Q_r]$ and an initial error of 10K in the nodes that influence the most the magnet temperature.

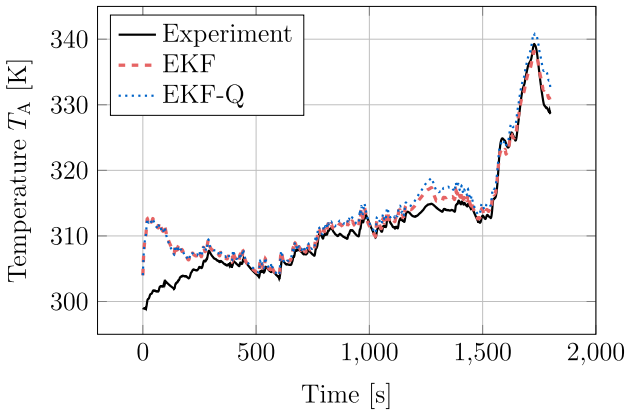

Fig. 23. PMSM: End-winding A temperature during a WLTP cycle with $\mathbf{Q} = [Q_r]$ and an initial error of 10K in the nodes that influence the most the magnet temperature.

These results show that uncertainty in several sources brings about a decrease in the accuracy of temperature estimation of the EKF-Q. The proposed method, however, is still able to correctly track temperature variations at locations where physical sensors cannot be placed and improves the behavior of a conventional EKF estimator.

3) Initial Temperature Error: In operation scenarios, the initial temperature of all the LPTN nodes is uncertain. Although an approximation can be obtained from sensor measurements, the exact temperature will depend on the previous working cycles, the resting time of the motor, and the temperature of the environment. In Section III-E, the effects of errors in the initial temperatures were tested, and the EKF-Q was able to correct the error over time. A similar test was performed in the experimental setup, increasing by 10K the initial temperature of the nodes with the most influence on magnet temperature, according to the results of the sensitivity analysis performed in [2]. Figs. 22 and 23 show the estimation of the magnet and end-winding A temperatures, respectively. It can be seen how, as in the benchmark case, the EKF-Q is able to overcome the initial error and converge to the measured temperatures.

V. Conclusion

The thermal behavior of electric powertrains has a direct impact on their performance. Knowing the internal temperatures of the electric drives used in these applications allows one to enhance their operation while avoiding damaging the device. However, in practice, it is not possible to install physical sensors to measure the temperatures at all the critical locations. Virtual sensing strategies can be used to address this issue, combining computational descriptions of the motor thermal dynamics with readings from those sensors that can actually be mounted on the monitored system. A common approach in virtual sensing for thermal effects is to use temperature readings for this end.

In this work, we put forward a virtual sensing strategy that uses power measurements to support temperature estimation. Such readings, namely the electric magnitudes that regulate motor operation, its rotational speed, and the torque that it delivers, can be obtained with conventional equipment in test benches for electrical motors. With these additional measurements, it is possible to develop a Kalman filter to estimate motor temperatures, using the power balance of the device as a sensor able to determine the overall heat flow inside the drive. The method builds upon a previously developed EKF that relied exclusively on temperature sensors to estimate LPTN parameters and internal temperatures in the motor. The new approach enhances the capabilities of the previous filter, making it more robust to uncertainties in heat source descriptions. The proposed strategy can be used to characterize the thermal behavior of systems with different topologies, providing predictions of thermal losses and internal temperatures. It can also be adapted for its use on on-board applications.

The method was first verified and illustrated by means of a simple benchmark example, a thermal *RC* circuit with two heat sources. It was confirmed that uncertain heat source values resulted in inaccurate results of the conventional filter, which were improved by the new method. Adding information regarding total heat losses helped the filter to improve heat source estimation, resulting in enhanced temperature estimations. The benchmark also showed that the accuracy of the estimated heat sources depends on the number of sensors and their location. Finally, the method was also tested under different levels of sensor noise and uncertainties in the initial temperatures of the system, yielding satisfactory results.

The new approach was validated in experimental tests with an automotive-grade PMSM. An LPTN description of the motor with uncertain heat sources was used to build an EKF that received temperature measurements from stator locations. Together with the power balance of the motor, it was possible to deliver more realistic estimations of the rotor magnet temperature and end-winding rack losses.

As future work, the sensitivity of the method to parameter uncertainties should be studied to provide a more reliable framework that can be applied in real-world applications.

References

[1] P. Milanfar and J. H. Lang, "Monitoring the thermal condition of permanent-magnet synchronous motors," *IEEE Trans. Aerosp. Electron. Syst.*, vol. 32, no. 4, pp. 1421–1429, Oct. 1996.

[2] J. García Urbieta, B. Rodríguez, A. J. Rodríguez, P. Díaz, S. Armentia, and F. González, "Sensitivity analysis of lumped-parameter thermal networks for the experimental calibration of eMotor models," *IEEE Trans. Transport. Electrific.*, vol. 10, no. 3, pp. 6210–6220, Sep. 2024.

[3] O. Wallscheid and J. Böcker, "Derating of automotive drive systems using model predictive control," in *Proc. IEEE Int. Symp. Predictive Control Electr. Drives Power Electron. (PRECEDE)*, Sep. 2017, pp. 31–36.

[4] P. N. Phuc, D. Bozalakov, H. Vansompel, K. Stockman, and G. Crevecoeur, "Rotor temperature virtual sensing for induction machines using a lumped-parameter thermal network and dual Kalman filtering," *IEEE Trans. Energy Convers.*, vol. 36, no. 3, pp. 1688–1699, Sep. 2021.

[5] D. E. G. Erazo, O. Wallscheid, and J. Böcker, "Improved fusion of permanent magnet temperature estimation techniques for synchronous motors using a Kalman filter," *IEEE Trans. Ind. Electron.*, vol. 67, no. 3, pp. 1708–1717, Mar. 2020.

[6] J. G. Urbieta, I. García, P. Díaz, S. Armentia, A. J. Rodríguez, and F. González, "Efficient calibration of LPTN models for digital twins of ePowertrain motors," in *Proc. 13th Int. Electr. Drives Prod. Conf. (EDPC)*, Nov. 2023, pp. 1–8.

[7] K. Fujisaki, Ed., *Handbook of Magnetic Material for Motor Drive Systems*. Singapore: Springer Nature, 2025.

[8] F. Fiorillo and A. Novikov, "An improved approach to power losses in magnetic laminations under nonsinusoidal induction waveform," *IEEE Trans. Magn.*, vol. 26, no. 5, pp. 2904–2910, Sep. 1990.

[9] A. Krings, J. Soulard, and O. Wallmark, "Influence of PWM switching frequency and modulation index on the iron losses and performance of slot-less permanent magnet motors," in *Proc. Int. Conf. Electr. Mach. Syst. (ICEMS)*, Oct. 2013, pp. 474–479.

[10] Z.-Q. Zhu et al., "Evaluation of iron loss models in electrical machines," *IEEE Trans. Ind. Appl.*, vol. 55, no. 2, pp. 1461–1472, Mar. 2019.

[11] S. Sirimanna, T. Balachandran, and K. Haran, "A review on magnet loss analysis, validation, design considerations, and reduction strategies in permanent magnet synchronous motors," *Energies*, vol. 15, no. 17, p. 6116, Aug. 2022.

[12] Z. Li et al., "Loss calculation and thermal analysis of ultra-high speed permanent magnet motor," *Heliyon*, vol. 8, no. 11, Nov. 2022, Art. no. e11350.

[13] J. Lee and J.-I. Ha, "Temperature estimation of PMSM using a difference-estimating feedforward neural network," *IEEE Access*, vol. 8, pp. 130855–130865, 2020.

[14] W. Kirchgässner, O. Wallscheid, and J. Böcker, "Data-driven permanent magnet temperature estimation in synchronous motors with supervised machine learning: A benchmark," *IEEE Trans. Energy Convers.*, vol. 36, no. 3, pp. 2059–2067, Sep. 2021.

[15] R. Hughes, T. Haidinger, X. Pei, and C. Vagg, "Real-time temperature prediction of electric machines using machine learning with physically informed features," *Energy AI*, vol. 14, Oct. 2023, Art. no. 100288.

[16] T. Sharifi, A. Eikani, and M. Mirsalim, "Heat transfer study on a stator-permanent magnet electric motor: A hybrid estimation model for real-time temperature monitoring and predictive maintenance," *Case Stud. Thermal Eng.*, vol. 63, Nov. 2024, Art. no. 105286.

[17] A. I. Ramones, B. Shi, M. Engels, M. Eisenbarth, and J. Andert, "Estimating the real-time temperature of a 48 V permanent magnet synchronous motor using a thermal neural network," *Energy Convers. Manage., X*, vol. 27, Jul. 2025, Art. no. 101140.
[18] G. Feng, C. Lai, J. Tjong, and N. C. Kar, "Noninvasive Kalman filter based permanent magnet temperature estimation for permanent magnet synchronous machines," *IEEE Trans. Power Electron.*, vol. 33, no. 12, pp. 10673–10682, Dec. 2018.
[19] J. Gao, C. Li, W. Zhang, and S. Huang, "Permanent magnet temperature estimation of high power density permanent magnet synchronous machines by considering magnetic saturation," *J. Power Electron.*, vol. 21, no. 12, pp. 1804–1811, Dec. 2021.
[20] D. F. Laborda, D. Reigosa, D. Fernández, K. Sasaki, T. Kato, and F. Briz, "Variable leakage flux permanent magnet synchronous machine PM temperature estimation based on PM flux linkage," *IEEE Access*, vol. 11, pp. 112620–112630, 2023.
[21] R. Brody, M. McIntyre, and B. Grainger, "Online permanent magnet temperature estimation in permanent magnet machines using nonlinear observer with enhanced parameter estimation to minimise risk of demagnetisation," *IET Electric Power Appl.*, vol. 19, no. 1, p. 70043, Jan. 2025.
[22] B. Rodríguez, E. Sanjurjo, M. Tranchero, C. Romano, and F. González, "Thermal parameter and state estimation for digital twins of E-powertrain components," *IEEE Access*, vol. 9, pp. 97384–97400, 2021.
[23] B. Rodríguez, F. González, M. Á. Naya, and J. Cuadrado, "Assessment of methods for the real-time simulation of electronic and thermal circuits," *Energies*, vol. 13, no. 6, p. 1354, Mar. 2020.
[24] R. Mehra, "Approaches to adaptive filtering," *IEEE Trans. Autom. Control*, vol. AC-17, no. 5, pp. 693–698, Oct. 1972.
[25] A. J. Rodríguez, E. Sanjurjo, R. Pastorino, and M. Á. Naya, "Multibody-based input and state observers using adaptive extended Kalman filter," *Sensors*, vol. 21, no. 15, p. 5241, Aug. 2021.
[26] A. J. Rodríguez, E. Sanjurjo, and M. Á. Naya, "An enhanced adaptive Kalman filter for multibody model observation," *Sensors*, vol. 25, no. 7, p. 2218, Apr.2025.

Pablo Díaz-Brage received the bachelor's degree in industrial engineer (specialty construction) from the University of A Coruña, Ferrol, Spain, in 2015.

Since 2015, he worked in numerical simulation applied to fluid mechanics, enjoying a scholarship with the Integrated Group of Engineering from University of A Coruña and later, from another with the Techno-logical Institute of Aragon, Zaragoza, Spain. Since February 2017, he oriented his activity toward life and sports sciences at the Faculty of Sports Sciences and Physical Education, UDC, A Coruña, Spain, defending his Ph.D. thesis in 2019, with a focus on digital acquisition and processing of biological signals. He joined the UDC Mechanical Engineering Laboratory (LIM), Ferrol, in April 2021, participating in biomechanics projects. After working at CTAG, O Porriño, Spain, and Jember Engineering Solutions, Madrid, Spain, he returned to LIM in August 2022, dedicating himself to multiphysics simulation of automotive electric motors. He is also actively collaborating on biomechanical applications.

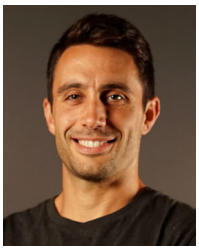

Antonio J. Rodríguez received the bachelor's degree in mechanical engineering from the University of A Coruña, Ferrol, Spain, in 2015, and the Ph.D. degree from the University of A Coruña, in 2020, with a focus on the implementation of state observers for automotive applications in embedded systems.

Since 2020, he has been working on applications of multibody dynamics to the automotive field and industrial machinery. His research interests include the application of Kalman filters and co-simulation techniques to mechanical systems.

Jon García-Urbieta received the B.S. and M.Sc. degrees in industrial engineering from the University of Navarra, San Sebastián, Spain, in 2016 and 2018, respectively, and the Ph.D. degree in industrial and naval engineering from the University of La Coruña, Ferrol, Spain, in 2024, with a focus on Digital Twins for the thermal analysis of PMSMs. He is currently pursuing an M.B.A. degree with IESE Business School, Madrid, Spain.

His master's thesis was as a visiting student and research assistant at the Space Propulsion Laboratory, MIT, Cambridge, MA, USA, with a focus on novel propellants for ion electrospray thrusters for CubeSats. He also works on the development of digital twins for driveline products and testbenches in Dauch (GKN Automotive, Zumaia, Spain).

Francisco González received the bachelor's degree in mechanical engineering from the University of Navarra, San Sebastián, Spain, in 2004, and the Ph.D. degree from the University of A Coruña, Ferrol, Spain, in 2010.

He held a post-doctoral position with McGill University, Montreal, QC, Canada, and the University of A Coruña, with a focus on simulation and analysis methods for robotics and mechanical systems. He is currently an Associate Professor at the Laboratory of Mechanical Engineering, University of A Coruña. His research interests include real-time simulation methodologies and co-simulation techniques for multiphysics applications.